Journal of Materials Science & Technology 114 (2022) 191–205

Contents lists available at ScienceDirect

Journal of Materials Science & Technology

journal homepage: www.elsevier.com/locate/jmst

Research Article

Stress-controlled fatigue of HfNbTaTiZr high-entropy alloy and associated deformation and fracture mechanisms

Shuying Chen[a], Weidong Li[b,*], Ling Wang[b], Tao Yuan[c], Yang Tong[a], Ko-Kai Tseng[d], Jien-Wei Yeh[d], Qingang Xiong[e,f], Zhenggang Wu[g], Fan Zhang[h], Tingkun Liu[b], Kun Li[i], Peter K. Liaw[b,*]

[a] Institute for Advanced Studies in Precision Materials, Yantai University, Yantai 264005, China
[b] Department of Materials Science and Engineering, The University of Tennessee, Knoxville, TN 37996, USA
[c] Department of Industrial and Systems Engineering, Ohio University, Athens, OH 45701, USA
[d] Department of Materials Science and Engineering, High Entropy Materials Center, National Tsing Hua University, Hsinchu, 30013, Taiwan, China
[e] State Key Laboratory of Pulp and Paper Engineering, South China University of Technology, Guangzhou 510640, China
[f] School of Light Industry and Engineering, South China University of Technology, Guangzhou 510640, China
[g] College of Materials Science and Engineering, Hunan University, Changsha 410082, China
[h] WPI Advanced Institute for Materials Research, Tohoku University, Sendai 980-8577, Japan
[i] State Key Laboratory of Mechanical Transmission, Chongqing University, Chongqing 400044, China

ARTICLE INFO

Article history:
Received 20 July 2021
Revised 7 October 2021
Accepted 8 October 2021
Available online 7 January 2022

Keywords:
Fatigue mechanisms
Intrinsic toughening
Extrinsic toughening
Probabilistic modeling

ABSTRACT

The stress-controlled fatigue tests are carried out at a stress ratio of 0.1 and a frequency of 10 Hz, and span both low-cycle and high-cycle regimes by varying the applied stress amplitudes. The high-cycle fatigue regime gives a fatigue strength of 497 MPa and a fatigue ratio of 0.44. At equivalent conditions, the alloy's fatigue strength is greater than all other high-entropy alloys (HEAs) with reported high-cycle fatigue data, dilute body-centered cubic alloys, and many structural alloys such as steels, titanium alloys, and aluminum alloys. Through in-depth analyses of crack-propagation trajectories, fracture-surface morphologies and deformation plasticity by means of various microstructural analysis techniques and theoretical frameworks, the alloy's remarkable fatigue resistance is attributed to delayed crack initiation in the high-cycle regime, which is achieved by retarding the formation of localized persistent slip bands, and its good resistance to crack propagation in the low-cycle regime, which is accomplished by intrinsic toughening backed up by extrinsic toughening. Moreover, the stochastic nature of the fatigue data is neatly captured with a 2-parameter Weibull model.

1. Introduction

The research in high-entropy alloys (HEAs) has been surging in recent years [1]. Great interests in this field are, to a large extent, provoked by their radical differences with traditional alloys. The most salient difference is their compositions. Traditional alloys usually comprise one or two principal elements as the solvent and a varying number of minor elements as solutes. On the other hand, by the original definition, all composing elements in HEAs are principal elements, with the concentration of each element varying between 5 at.% and 35 at.% [2]. In other words, there is no distinction between the solvent and solutes. Reflected on phase diagrams, the vast majority of traditional alloys are located at corners with some at edges, whilst HEAs occupy the enormously large, uncharted central region. The second crucial difference is alloy thermodynamics. Simply put, the mixing of enthalpy dictates the design of conventional alloys, whereas the mixing of entropy is maximized in HEAs to stabilize their microstructures [2–4]. As a result of these two differences, HEAs were reported to exhibit many intriguing mechanical properties rarely seen before in traditional alloys. Examples include the balanced strength and ductility in metastable HEAs [5], retained fracture toughness at cryogenic temperatures in face-centered-cubic (fcc) HEAs [6], retained high-strength at elevated temperature in body-centered-cubic (bcc) HEAs [7], good creep properties [8–10], remarkable fatigue resistance [10,11], among others.

Due to the great promise in structural applications, the mechanical properties of HEAs have been of major interest since their emergence [12–14]. In early work, the focus was mainly on

* Corresponding authors.
E-mail addresses: wli20@utk.edu (W. Li), pliaw@utk.edu (P.K. Liaw).

https://doi.org/10.1016/j.jmst.2021.10.026
1005-0302/

basic properties, such as hardness, strength, and ductility [13–15]. As research is gradually geared toward engineering applications [16–18], fatigue is receiving increasing attention. This is because in practice a large portion of metal structures is subject to cyclic loading rather than simple static loading, not to mention that approximately 90% of engineering structures are in fact failed by fatigue [19]. Over past several years, low-cycle fatigue [20,21], high-cycle fatigue [22–33], and fatigue crack growth rates [34–38] of a variety of HEAs have been investigated. Among these investigations, high-cycle fatigue with the stress-life method prevails given its closeness to actual loads undergone by most engineering structures. HEAs whose high-cycle fatigue behaviors have been examined include the fcc CoCrFeMnNi and its variants [22–27], $Al_{0.5}CoCrCuFeNi$ with two fcc phases [39,40], metastable $Fe_{42}Mn_{28}Cr_{15}Co_{10}Si_5$ and $Fe_{38.5}Mn_{20}Co_{20}Cr_{15}Si_5Cu_{1.5}$ with a fcc to hexagonal-close-packed (hcp) martensitic transformation [28,29], eutectic $AlCoCrFeNi_{2.1}$ [30], duplex $Al_{0.7}CoCrFeNi$ [32], triplex $Al_{0.3}CoCrFeNi$ and $Al_{0.7}CoCrFeNi$ [31,32], and bcc HfNbTaTiZr [41].

Refractory bcc HEAs are a subclass of HEAs that are of particular interest due to their compelling high-temperature strengths and the likelihood of being the replacement materials of Ni-based superalloys in the aerospace industry [42,43]. Unfortunately, compared to other types of HEAs, the fatigue behaviors of refractory HEAs are rarely investigated and poorly understood, despite some attempts [36,41]. More importantly, fatigue mechanisms in bcc HEAs were not clearly and satisfactorily revealed. Undoubtedly, the lack of adequate knowledge about the fatigue behavior of refractory bcc HEAs impedes the all-around assessments of their suitability in structural applications.

In consideration of the pressing need, the present work aims to provide a comprehensive understanding of the fatigue behavior of refractory bcc HEAs through utilizing the HfNbTaTiZr as a model material [12,44]. The objectives of the present work are threefold. Firstly, conduct stress-controlled fatigue tests on the HfNbTaTiZr to obtain its low-cycle and high-cycle fatigue behaviors and compare its fatigue strength with those of other alloy systems. Secondly, reveal fatigue mechanisms in the HfNbTaTiZr via various forms of microstructural probing. Thirdly, perform statistical modeling to capture the probabilistic nature of the fatigue behavior of the alloy.

2. Experimental

2.1. Material

The HfNbTaTiZr ingots were prepared by arc-melting high purity elements (99.9 wt.%) in an argon atmosphere with at least five times of flipping and re-melting, and then drop-casting in a water-cooled copper mold. All ingots, after being cut into $13.5 \times 25 \times 50$ mm^3 plates, were cold-rolled with a thickness reduction of 70%. The cold-rolled sheets were then sealed in vacuum quartz tubes, annealed in an air furnace at 1200 °C for 10 min, and quenched in water.

2.2. Mechanical tests

The specimens of two different shapes are machined out of the annealed sheets, with their longitudinal direction parallel to the rolling direction. The dog-bone-shaped tensile samples have a full dimension of $46 \times 9.5 \times 1$ mm^3 and a gage section of $20 \times 3 \times 1$ mm^3, whereas the cuboidal fatigue specimens have a dimension of $25 \times 3 \times 3$ mm^3. Prior to tests, all specimens were ground and polished on a Buehler rotating grinder and polisher to remove surface imperfections incurred during fabrication and processing. For this purpose, SiC papers of 240, 400, 600, and 1200 grits were used in order.

Tensile tests were conducted on an Instron 4505 machine at room temperature and a strain rate of 1×10^{-3} s^{-1}. The tests were repeated for three times for data repeatability. The fatigue of the HfNbTaTiZr alloy was fullfilled with the cyclic four-point bending tests on a computer-controlled servo-hydraulic testing machine. A series of loads, in the form of sinusoidal waves, was applied at a frequency of $f = 10$ Hz, and a nominal stress ratio of $R = \sigma_{\min}/\sigma_{\max} = 0.1$, where $\sigma_{\min}$ and $\sigma_{\max}$ are the minimum and maximum applied stresses, respectively. Fatigue runs were deemed complete if either a sample failed or 1×10^7 fatigue cycles were reached. According to the classic elastic beam bending theory, the maximum stress on the tensile surface of a cyclically bent specimen is first estimated by Hemphill et al. [39]

$$\sigma_{\max,el} = \frac{3P(S_o - S_i)}{2BW^2}, \tag{1}$$

where P is the applied load, B is the sample thickness, W is the sample width, S_o and S_i are the outer and inner spans of the sample, respectively, which are 20 mm and 10 mm in our case. However, the maximum stresses computed from Eq. (1) in many samples are proven to exceed the yield strength of the alloy, signaling the occurrence of plastic deformation in these samples. By considering the elastoplastic constitutive law of the alloy, the overestimated elastic maximum stresses are corrected to the realistic elastoplastic stresses with the Neuber method, as elaborated in Section 3.2.2.

2.3. Microstructural characterizations

Microstructural characterizations with high-energy X-ray diffractions (XRDs) were performed on the 11-ID-C beamline with a beam energy of 115.27 keV at the Advanced Photon Source (APS) of the Argonne National Laboratory. Back-scattered electron (BSE) imaging and energy-dispersive X-ray spectroscopy (EDS) were conducted on a Zeiss EVO MA15 scanning electron microscope (SEM) with an accelerating voltage of 20 kV. The electron backscattered diffraction (EBSD) measurements were carried out using the Bruker eFlash Electron Backscattered Detector. The transmission electron microscopy (TEM) samples were prepared via focused ion beam (FIB) lift-out techniques with Ga^+ ions at 30 kV and finishing energy of 5 kV using a Zeiss Crossbeam Auriga FIB-SEM system. The bright-field scanning transmission electron microscopy (BF-STEM) micrographs were taken by a JEOL 2100F equipped with double spherical aberration correctors at 200 kV.

3. Experimental results

3.1. Initial microstructures

The synchrotron XRD diffraction pattern of the as-annealed HEA is provided in Fig. 1(a), in which the seven indexed diffraction peaks all belong to a bcc crystal structure. No extra minor peaks or peak splitting is noted, indicative of the absence of any extra detectable phases. The lattice constant calculated from the XRD diffraction data is $a = 3.408$ Å, in good agreement with 3.406 Å reported in Ref. [45], 3.404 Å in Ref. [43], and 3.409 Å calculated by the Vegard's law [43]. The TEM micrograph of the as-annealed HEA at a randomly selected area in Fig. 1(b) discloses the pre-existence of curvy dislocations, though the density is low. The selected area diffraction pattern (SADP) in the inset reaffirms that the alloy has a single bcc crystal structure.

From an EBSD snapshot in Fig. 2(a), it is obvious that the as-annealed HEA consists of equiaxed grains of random orientation, with an average grain size of 45 ± 7 μm. The EDS mappings of all five constituent elements at a typical microstructure

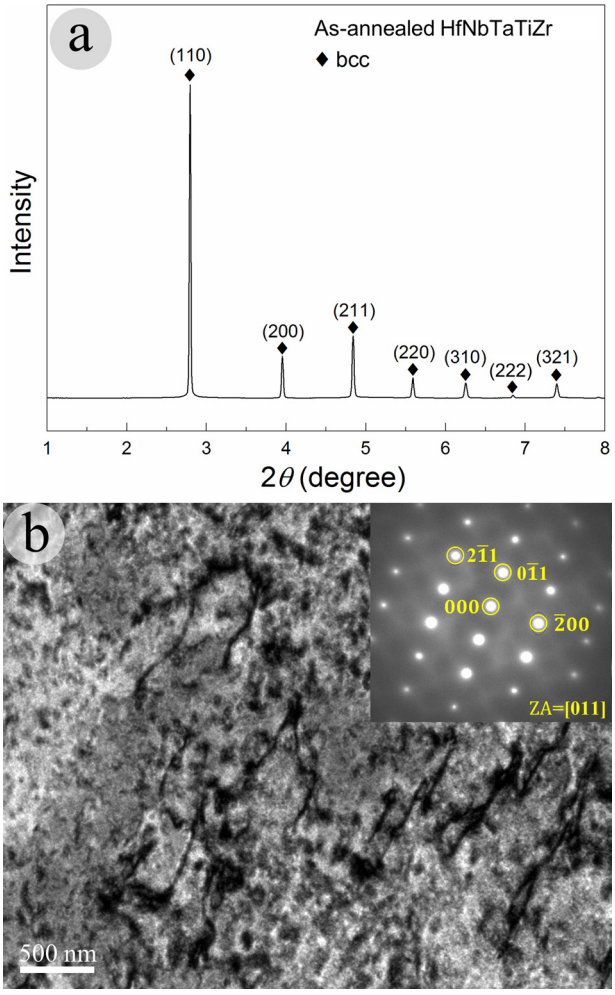

Fig. 1. (a) Synchrotron XRD diffraction pattern of the as-annealed HfNbTaTiZr HEA, indicating a body-cubic-centered (bcc) crystal structure with a lattice constant of $a = 3.408$ Å. (b) TEM micrograph of the as-annealed HEA at a randomly selected area revealing pre-existing dislocations. The selected area diffraction pattern (SADP) in the inset reaffirms a bcc structure.

domain (the first sub-figure) are given in Fig. 2(b), from which it is seen that all alloying elements are uniformly distributed, without any sign of elemental segregation or formation of additional phases.

3.2. Mechanical properties

3.2.1. Uniaxial tension

A representative engineering stress-strain curve under tension, along with the converted true stress-strain curve, of the as-annealed HfNbTaTiZr obtained at room temperature and a strain rate of 1×10^{-3} s^{-1} is presented in Fig. 3(a). From the engineering stress-strain curves, the Young's modulus, offset yield strength, ultimate tensile strength, uniform elongation, and elongation at failure are determined to be $E = 38 \pm 3$ GPa, $\sigma_y = 1113 \pm 48$ MPa, $\sigma_{UTS} = 1139 \pm 42$ MPa (true stress of 1194 MPa), $e_u = 0.048 \pm 0.004$, and $e_f = 0.16 \pm 0.016$, respectively.

The Considere's construction is employed to determine the onset of necking. The construction is based on the necking instability criterion, $\frac{d\sigma}{d\varepsilon} = \sigma$, where σ and ε represent the true stress and true strain, respectively [46]. This criterion states that necking emerges when the true stress, σ, in a material equals its strain hardening rate, $\frac{d\sigma}{d\varepsilon}$. To use this criterion, we plot the strain-hardening rate together with the true stress as a function of the true strain in Fig. 3(b). Since it is unsure to what strain level that the standard conversion between the engineering and true stress-strain relations, i.e., $\varepsilon = \ln(e+1)$ and $\sigma^T = \sigma^E(e+1)$, is valid to use at the beginning, we choose to apply this standard conversion at a great strain level (~ 0.12) first and then gray out the invalid portion after knowing the exact necking location. By this approach, the necking is determined to initiate at a true strain of $\varepsilon_u = 0.044$, corresponding to an engineering strain of $e_u \approx 0.045$, as indicated in Fig. 3(b).

3.2.2. Fatigue

The elastic $\sigma_{max,el}$ of all fatigue samples calculated with Eq. (1) is listed in Table 1. It is noted that all $\sigma_{max,el}$ values already surpass the average offset yield strength of 1113 MPa, indicating that the elastic stress estimation with Eq. (1) is no longer appropriate in this circumstance due to induced plastic deformation. To obtain close-to-realistic maximum stresses on the samples, we here choose the Neuber method to correct for plasticity. The Neuber method equates the strain energy density of a simplified linear elastic material with that of an actual elastoplastic material, i.e.,

$$\frac{\sigma_{LE} \cdot \varepsilon_{LE}}{2} = \frac{\sigma_{EP} \cdot \varepsilon_{EP}}{2}, \tag{2}$$

where σ_{LE} and ε_{LE} denote the elastic stress and strain, whereas σ_{EP} and ε_{EP} plastic counterparts. The method is graphically illustrated in Fig. 4(a). An overestimated elastic stress (e.g., black dot) can be corrected back to an elastoplastic stress (e.g., red dot) lying on the elastoplastic stress-strain curve of the material along the line of constant strain energy density. To facilitate the pin-

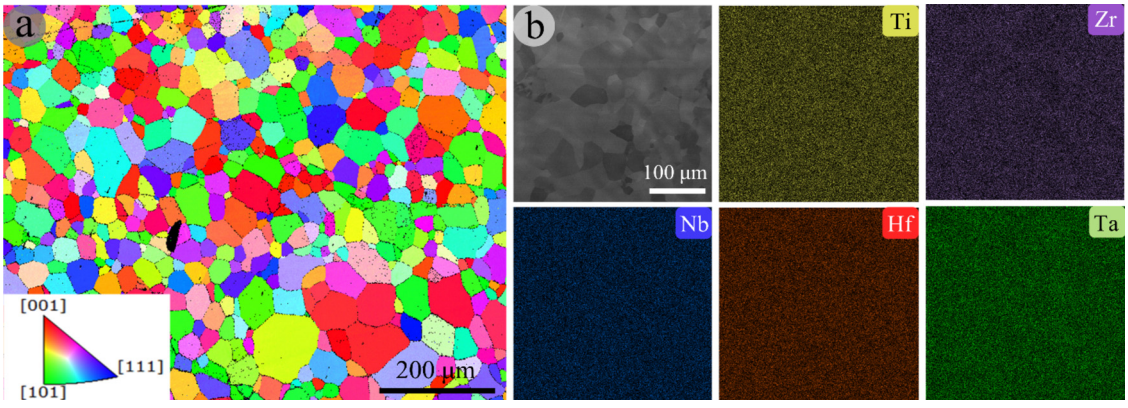

Fig. 2. (a) EBSD map of randomly oriented equiaxed grains with an average grain size of 45 ± 7 μm. (b) EDX mapping of all five constituent elements in a typical microstructure domain (the first sub-figure), ruling out the possibility of elemental segregation and formation of additional phases.

Table 1
Ultimate fatigue maximum stress, σ_{max}, stress ratio, R, and stress amplitude $\sigma_a = 0.5(1-R)\sigma_{max}$, corrected from $\sigma_{max,el}$ with the Neuber method, along with the as-read σ_{min} and N_f. All stresses are true stresses.

Sample ID	$\sigma_{max,el}$ (MPa)	σ_{max} (MPa)	σ_{min} (MPa)	σ_a (MPa)	R	N_f
1	1130	1106	113.0	496.63	0.10	1.00E7
2	1135	1110	113.5	498.41	0.10	1.00E7
3	1138	1113	113.8	499.49	0.10	1.00E7
4	1140	1114	114.0	500.21	0.10	96,200
5	1145	1119	114.5	502.01	0.10	107,553
6	1150	1123	115.0	503.83	0.10	148,868
7	1160	1131	116.0	507.48	0.10	40,000
8	1170	1137	117.0	509.77	0.10	120,547
9	1175	1139	117.5	510.55	0.10	34,041
10	1200	1149	120.0	514.51	0.10	275,792
11	1300	1179	130.0	524.58	0.11	23,395
12	1350	1184	135.0	524.30	0.11	18,735

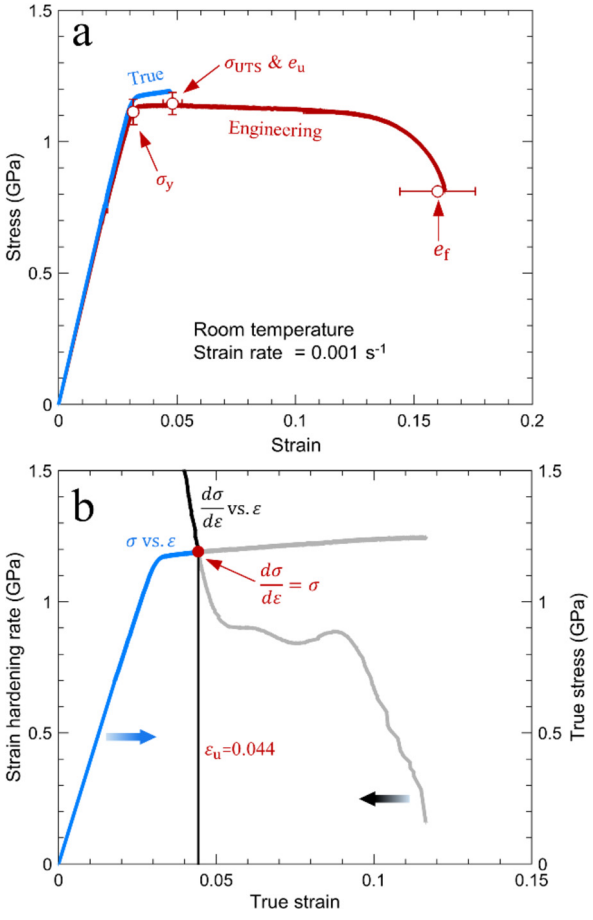

Fig. 3. (a) A representative engineering stress-strain curve and the corresponding true stress-strain curve of the HfNbTaTiZr HEA at room temperature and a strain rate of 1×10^{-3} s^{-1}. The average yield strength (σ_y), ultimate tensile strength (σ_{UTS}), uniform elongation (e_u) and fracture elongation (e_f) obtained from three different tests are superimposed as circular markers. (b) The Considere's construction in the strain hardening rate and true stress versus true strain for determining the onset of necking.

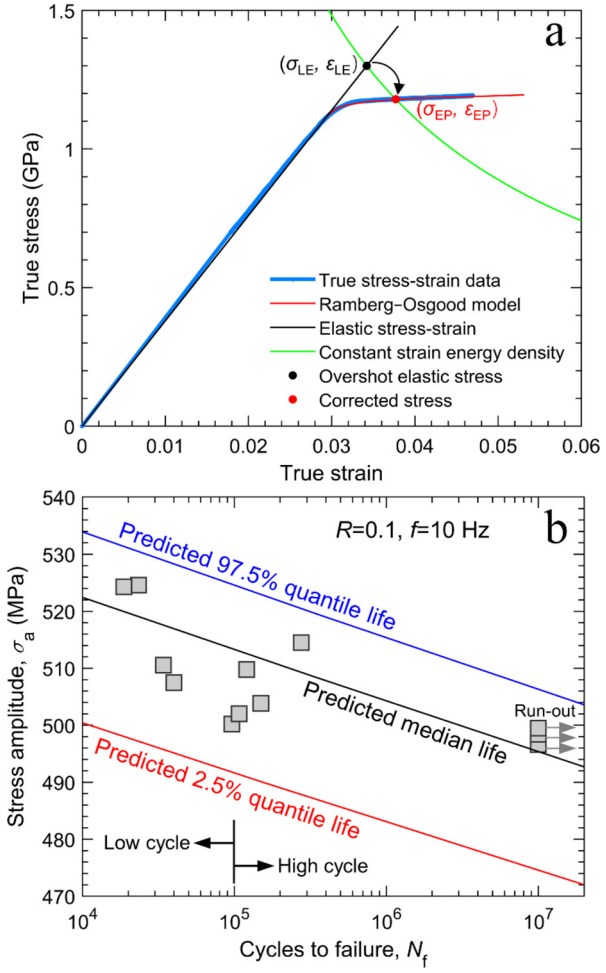

Fig. 4. (a) Illustration of the Neuber method for correcting an overestimated elastic stress to a realistic elastoplastic stress. (b) Experimentally recorded stress amplitude (σ_a) against the number of cycles to failure (N_f) along with the Weibull probabilistic modeling (lines).

point of the intercept where the line of constant strain energy density crosses the elastoplastic stress-strain curve, the Ramberg-Osgood model, $\varepsilon = \frac{\sigma_{UTS}}{E} + 0.002(\frac{\sigma_{UTS}}{\sigma_y})^n$, is first fit to the experimental true stress-strain data, where n is the only free parameter. With this methodology, the maximum stress, σ_{max}, stress amplitude, $\sigma_a = (\sigma_{max} - \sigma_{min})/2$, and R of all samples are corrected and documented in Table 1. Note that the minimum stress, σ_{min}, need not be corrected given all initially applied stresses stay well below yield strength.

The corrected σ_a of the bcc HfNbTaTiZr HEA is then plot against the number of cycles to failure, N_f, on a logarithmic scale in Fig. 4(b) with a standard stress-life method ($S-N$ method). Fig. 4(b) is, in fact, consisted of low-cycle and high-cycle regimes, as delimited by at 10^5 cycles.

The fatigue data overall are rather scattered, likely caused by internal microstructural defects [39]. In the high-cycle regime, the

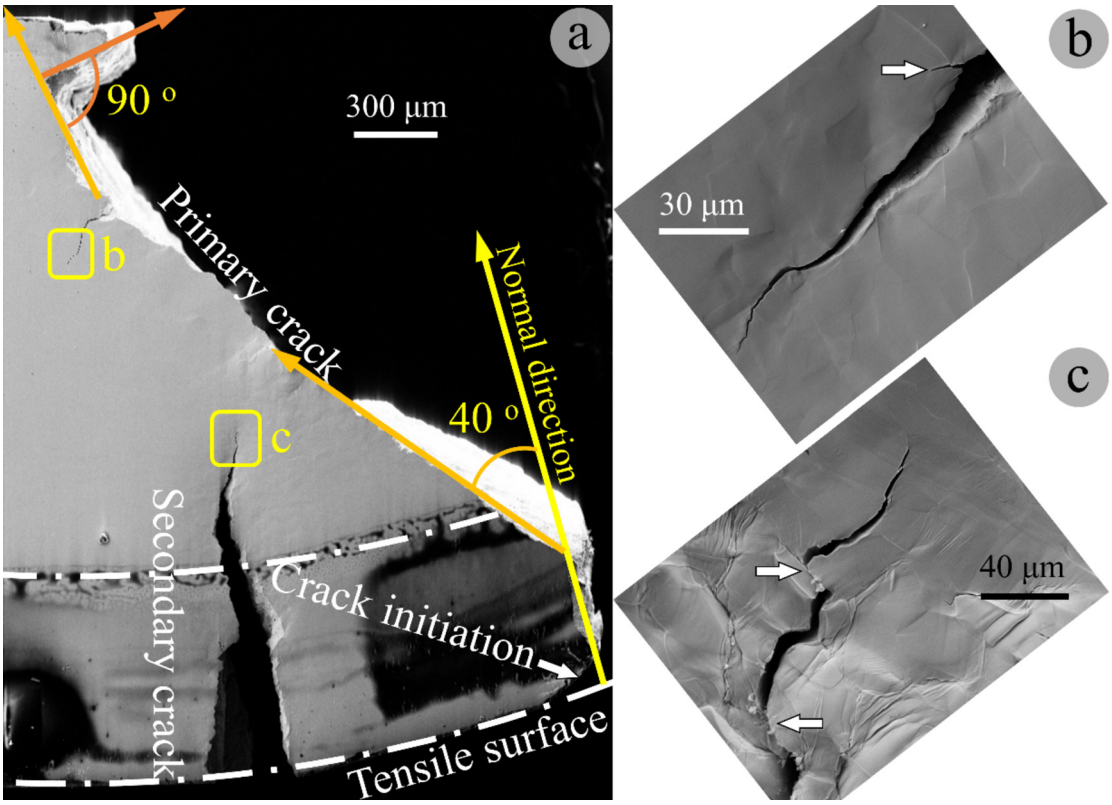

Fig. 5. (a) SEM image of a representative fatigue-failed half sample, failed at $\sigma_{max} = 1137$ MPa and $N_f = 120,547$, showing crack deflection on the primary crack and a secondary crack initiating also from the tensile side of the bending sample. The long arrows are indicative of crack-propagation directions. (b) Magnified micrograph of the crack tip of a crack branched from the primary crack, indicating hierarchical crack branching. (c) Magnified micrograph of the tip of the secondary crack, exhibiting crack interlocking resulting from frequent crack deflection.

fatigue strength, which is usually defined as the stress amplitude at 10^7 fatigue cycles, is a crucial index used to judge the fatigue resistance of a material. When the applied stress amplitude during cyclic loading is below the fatigue strength of a material, it is believed that the fatigue life of the material is remarkably long. The fatigue strength of the alloy at a stress ratio of $R = 0.1$ in the present work is determined to be approximately $\sigma_{af} = 497$ MPa. With the ultimate tensile strength of $\sigma_{UTS} = 1139$ MPa, its fatigue ratio is calculated to be $\sigma_{af}/\sigma_{UTS} = 0.44$.

3.3. Low-cycle fatigue characteristics

3.3.1. Crack-propagation trajectories

The first glance of propagation trajectories of all cracks in nearly all fatigue-failed HEA samples reveals a number of salient characteristics. First, all primary cracks deviate their propagation paths from the plane normal to the global maximum tensile stress, i.e., the vertical centerline of the four-point-bending fatigue samples. Second, besides the primary crack, each sample sees a multitude of secondary cracks of varying lengths initiating from the same side as the primary crack but terminating in the interior of the sample. Their growth directions are not necessarily parallel to the primary crack or normal to the global maximum tensile stress. Third, some short cracks are noticed to branch from primary and secondary cracks, which we refer to as derived or branched cracks. Fourth, many primary, secondary, and derived cracks manifest serrated fracture profiles. In what follows, we will digest in detail these features by representatively examining a primary crack and then some secondary and derived cracks.

A representative fatigue-failed half sample is present in Fig. 5(a), from which all four characteristics suggested beforehand can be seen. The primary crack initiates from the tensile side of the bending sample and propagates in the direction normal to the global maximum tensile stress at the beginning. After propagating a distance of ~500 μm, the crack growth turns to a path that is deviated by ~40° from the starting path. The deflected crack continues to grow until reaching the final stage of propagation, where it makes another sharp deflection of ~90° to form a large serration.

Similar to the primary crack, the secondary crack in Fig. 5(a) also propagates in the direction normal to the global maximum tensile stress at the beginning, but the deviation sets in at ~ 500 μm, as marked by the first serration on its halfway in Fig. 5(a). The enlarged crack tip in Fig. 5(c) reveals more frequent crack deflections, which create closely spaced serrated crack faces that are interlocked at the action of a mode-II shear displacement, as indicated by the arrows.

A side crack derived from the primary crack is magnified and shown in Fig. 5(b). It is seen that on this first-level derived crack, another short side crack branches out to form a second-level derived crack, as indicated by the arrow. As a consequence, a hierarchical crack branching mechanism is essentially in play in the present alloy to dissipate the potential energy remarkably and retard fatigue crack propagation, though the extent and size of each level of crack branching are not vastly extensive.

Another secondary crack beside the primary crack, with the position shown in the inset of Fig. 6, is selected for further analyses. A panoramic view of the full crack propagation trajectory is created by adjoining the SEM images of the crack path at different locations and is given in Fig. 6. Likewise, the crack initiates from the tensile surface of the bending sample, propagates ~ 20 μm in the direction normal to the global maximum tensile stress, and then deviates to a path that makes ~ 40° with the initial propagation direction. Throughout the full crack propagation, some marked

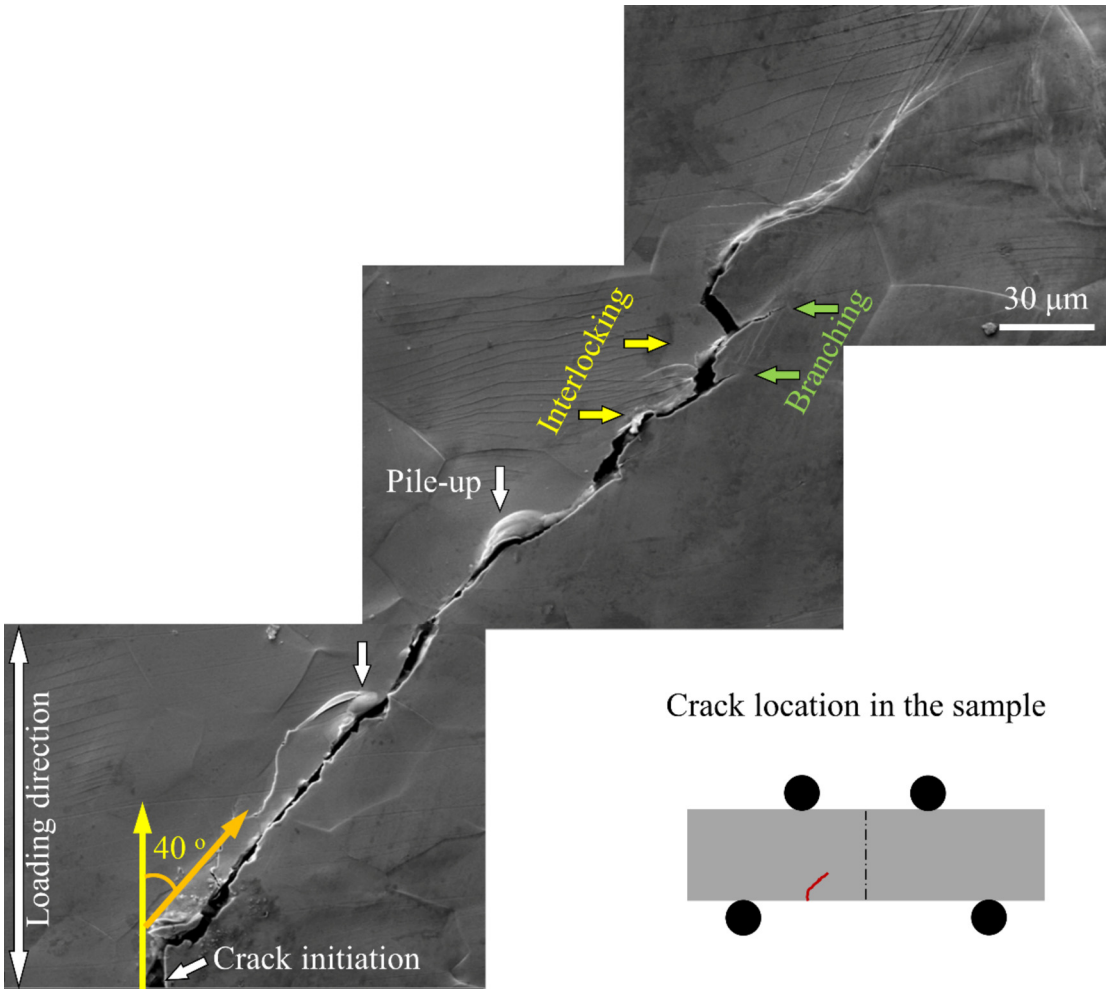

Fig. 6. Adjoined SEM images of the sample failed at $\sigma_{max} = 1149$ MPa and $N_f = 275792$, showing the full propagation trajectory of another secondary crack, from which crack deflection, crack interlocking, crack branching, and crack closure (indicated by the pile-ups) are noticed. The long arrows are indicative of crack-propagation directions.

characteristics are noticed: (1) Crack closure has taken place at multiple places, as implied by the pile-ups stemming from the plastic deformation of crack faces. (2) Near the crack tip, the tortuous or serrated crack path, generated from crack deflection and meandering, tends to interlock the two crack faces at the action of the shear from the mode-II fracture component. (3) Crack branching is noted to accompany crack deflection at locations near the crack tip. These observations basically confirm the widespread appearance of crack deflection, crack interlocking, and crack branching in the HfNbTaTiZr during low-cycle fatigue.

Fig. 7, the enlarged view of a segment of one another secondary crack, shows more pronounced serrations on the fracture faces. These crack serrations, incurred by frequent and uninterrupted crack deflections, constitute a tortuous crack-propagation trajectory and create remarkable roughness on the fracture surfaces. These serrated crack surfaces can too become interlocked at the action of the mode-II shear to engender a potent extrinsic toughening mechanism – roughness-induced crack closure. In this scenario, the mode-II shear is evidenced from the mismatch between the two mating fracture faces, while the occurrence of the roughness-induced crack closure is signified by the bumped ledges on the fracture faces at the lower half of Fig. 7(a).

Another strong evidence of pronounced crack branching in the alloy under examination is given in Fig. 7(b). Many short cracks branch out sideways from a secondary crack as it propagates, with some exhibiting hierarchical characteristics. From the fracture mechanics standpoint, extensive crack branching allows the released potential energy to be dissipated by much greater areas of crack surfaces [47]. In such a way, the propagation of the main crack is substantially impeded.

Furthermore, another potent crack shielding mechanism – debris wedging, which is commonly reported in the corrosion fatigue of metallic materials [48–50], is also observed in the plain fatigue of the present HEA, as representatively shown in Fig. 7(c). The wedging effect in corrosion fatigue is normally achieved through oxidation debris [48,49,51]. Differently, the debris in the present HEA is generated by a crack branching and remerging process, also promoted by crack deflection, as clearly observed from Fig. 7(c).

The serrated crack surfaces discussed above all result from crack propagation and deflection in a transgranular manner. This type of crack surfaces may also form from the intergranular fracture of the alloy along grain boundaries. Such an example is displayed in Fig. 8. In this example, the intergranular fracture occurs along a path perpendicular to the primary crack, causing serrated fracture surfaces at the resolution of grain sizes. It is worth noting that since the displayed segment of the primary crack is not at a location with its orientation perpendicular to the global maximum tensile stress, the derived intergranular crack is actually under a mixed-mode fracture. As discussed before, the action of the model-II shear on the serrated crack surfaces can lead to their interlocking, inducing an extrinsic toughening mechanism known as roughness-induced crack closure.

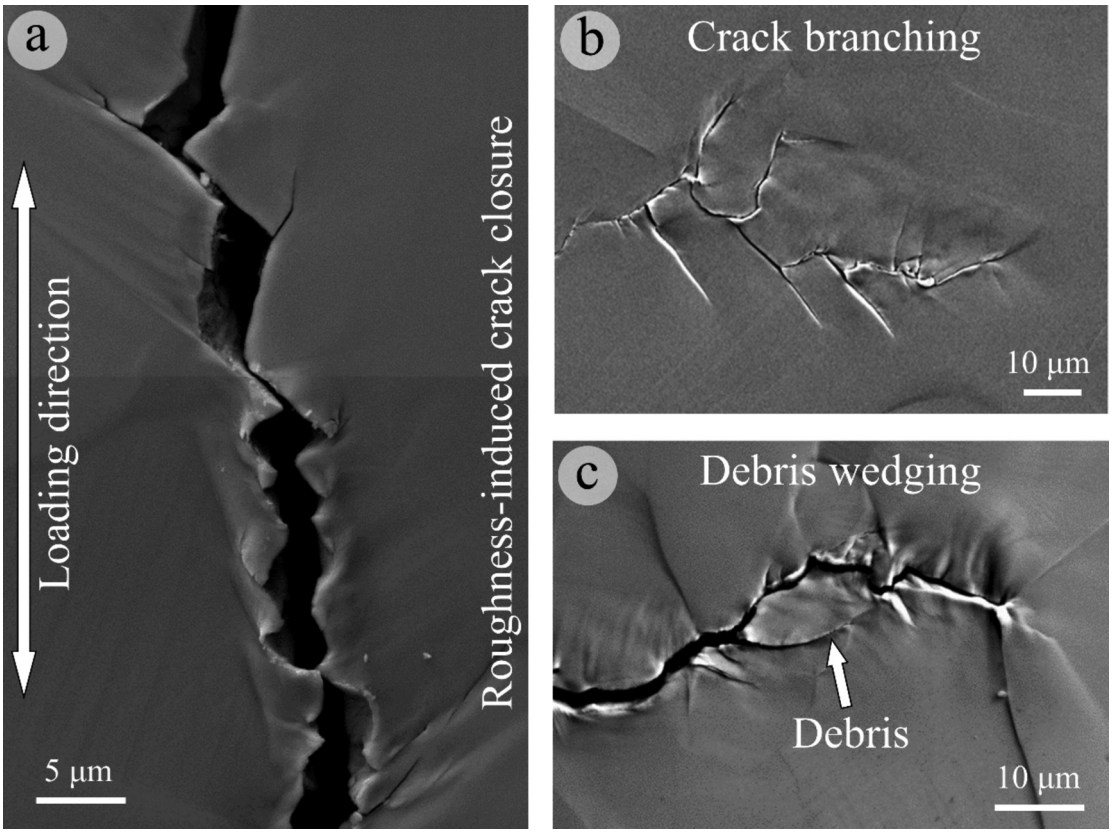

Fig. 7. SEM images of the secondary crack segments of the sample failed at $\sigma_{max} = 1123$ MPa and $N_f = 148868$, showing (a) pronounced serrations on the crack surfaces by transgranular crack deflection and crack interlocking by the action of the mode-II shear, (b) extensive crack branching near the crack tip with some branched cracks exhibiting hierarchical characteristics, (c) debris wedging behind the crack tip.

3.3.2. Fracture-surface morphologies

The microscopic observation of the failed half surface in Fig. 9(a) shows that, following crack initiation at the sample surface, the fatigue crack propagation in the HfNbTaTiZr HEA is constituted typically of three stages, i.e., stage I of slow crack propagation, stage II of incremental crack propagation, and stage III of rapid crack propagation. Micro-cracks initiated from the sample surface at the site of stress concentration propagate slowly along crystallographic planes in stage I where the resolved shear stress is high, ultimately resulting in the faceted fracture surface displayed in Fig. 9(c). Micro-cracks join to form one or more macro cracks in stage II, which turn to propagate in the direction perpendicular to the applied normal stress. The magnification of one area in the stage-II morphology reveals the formation of many micro cracks as a consequence of crack branching or meandering from the main crack, as indicated by the inset of Fig. 9(a). The magnification of another area, shown in Fig. 9(b), exposes the formation of apparent striations (or cleavage steps) in this stage. Of a single striation, the presence of two-level, finer striations is noticed, as given in the inset. The hierarchical striations are inferred to be originated from a two-stage process of blunting and sharpening of the crack tip [52]. The crack propagation in stage III is fast and is characteristic of intergranular fracture with localized dimples, as shown in Fig. 9(d).

Two more magnified views of the selected regions in stage II are given in Fig. 10(a) and (b). Both images contain abundant fatigue striations. Nevertheless, the sizes of striations in these two cases are different. The striations in Fig. 10(a) are very fine with a spacing of $\sim$ 0.5 μm, whereas coarse striations with a spacing of $\sim$15 μm are noted in Fig. 10(b). Since striations are the fingerprint of fatigue crack growth, differently spaced striations are indicative of the propagation of multi-level cracks, which could stem from crack branching and meandering. In fact, secondary cracks are noticed to form across fine striations in Fig. 10(a) and between coarse striations in Fig. 10(b).

3.3.3. Deformation near cracks

To understand the significance of plasticity involved during fatigue, it is interesting to examine the deformation of the alloy at locations near cracks at a micro level. With SEM, the first location examined is in the close vicinity of the main crack. From the overview image in Fig. 11(a), it is seen that the alloy has been severely strained near the main crack so that grains become staggered and are rather visible. A close-up view of a few grains in Fig. 11(b) reveals a very high density of slip lines. In two neighboring grains in Fig. 11(c), extrusions are noticed to form from persistent slip bands. In the region somewhat away from the crack, dense, rectilinear slip traces are also observed, as evidenced by the SEM image in Fig. 11(d), signaling planar slip.

Subtle dislocation substructures involved in fatigue are further disclosed by bright-field STEM and TEM imaging in the vicinity of the crack tip, as presented by a series of micrographs in Fig. 12. Under a two-beam condition, the TEM image in Fig. 12(b) was taken with $g = \{110\}$ and zone axis $\approx \langle 001 \rangle$, whereas the STEM images in the remaining sub-graphs were obtained with $g = \{10\bar{1}\}$ and zone axis $\approx \langle 111 \rangle$. These dislocation substructures comprise a large amount of heterogeneous dislocation tangles in the short, wavy form in Fig. 12(a), dislocation cells separated by walls in Fig. 12(b), dislocation loops in Fig. 12(c), dislocation arrays in Fig. 12(d), dislocation network consisted predominantly of hexagonal cells in Fig. 12(e), and dislocation network composed predominantly of parallelogrammatic cells in Fig. 12(f).

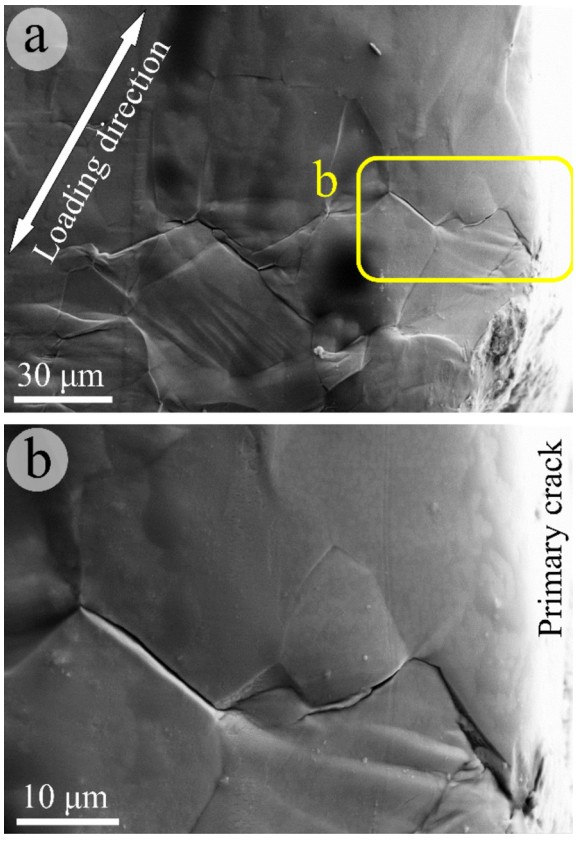

Fig. 8. (a) SEM image of a crack derived from the primary crack (location marked), manifesting serrated fracture surfaces formed from the intergranular fracture, the sample failed at $\sigma_{max} = 1179$ MPa and $N_f = 23395$. (b) Enlarged view of (a) confirming the intergranular fracture. Note that the primary crack is not perpendicular to the global maximum tensile stress. Therefore, the derived crack is experiencing a mixed-mode fracture.

In a recent work, it was suggested that rectilinear dislocations in the HfNbTaTiZr HEA are classical $\frac{a}{2}\langle 111\rangle$ screw dislocations, gliding primarily on {110} and {112} planes but also likely on other intermediate planes between these two families of planes [53]. In α-iron with a bcc structure, dislocation networks of hexagonal cells form as a result of two $\frac{a}{2}\langle 111\rangle$ dislocation joining to create a $a\langle 100\rangle$ dislocation (i.e., $\frac{a}{2}[1\bar{1}1] + \frac{a}{2}[11\bar{1}] \rightarrow a[100]$) or two $a\langle 100\rangle$ dislocations joining to make a $a\langle 110\rangle$ dislocation (i.e., $a[100] + a[010] \rightarrow a[110]$), whereas dislocation networks of parallelogrammatic cells are just the projections of the dislocation networks of hexagonal cells on planes other than {110} [54]. The dislocation networks formed in the present HfNbTaTiZr are expected to have similar origins. The prevalent rectilinear characteristic of screw dislocations in the HfNbTaTiZr was believed to be originated of the blocking of obstacles to cross slip and indicative of uneasy dislocation glide [53].

3.4. High-cycle fatigue characteristics

The microstructures of the specimen fatigue-failed in the high-cycle regime, i.e., $\sigma_{max} = 1119$ MPa and $N_f = 107,553$, are presented in Fig. 13. It is seen that the primary crack initiates at the lower right corner of the specimen and propagates upwards, during which intragranular tearing prevails with occasional intergranular cracking. Slip lines in grains adjacent to the primary crack are noted in Fig. 13(b,c), as marked by the yellow arrows. Secondary crack forms by branching out from the primary crack, as indicated by the green arrows in Fig. 13(c).

4. Statistical modeling

Fatigue is stochastic in nature and probabilistic modeling is oftentimes used for fatigue life prediction [19,55]. Among a wide variety of statistical models, the Weibull distribution is versatile and has been widely used for describing lifetime distributions in reliability engineering, fracture, and fatigue [55–58]. The present work attempts to use the 2-parameter Weibull distribution to model the fatigue life (N) distribution of the HfNbTaTiZr HEA, which depends on the applied stress amplitude (σ_a).

The probability density function (pdf) of the fatigue life, N, in a standard 2-parameter Weibull distribution is given as

$$f(N;\ \lambda, \kappa) = \begin{cases} \frac{\kappa}{\lambda}\left(\frac{N}{\lambda}\right)^{\kappa-1} \cdot \exp\left[-\left(\frac{N}{\lambda}\right)^{\kappa}\right] & N \geq 0 \\ 0 & N < 0 \end{cases} \tag{3}$$

where $\kappa > 0$ is the shape parameter and $\lambda > 0$ is the scale parameter of the distribution. As the fatigue life, N, cannot be negative, only the first term at $N \geq 0$ in Eq. (3) needs to be kept for fatigue life prediction. The corresponding cumulative distribution function (cdf) at $N \geq 0$ is given as

$$F(N;\ \lambda, \kappa) = 1 - \exp\left[-\left(\frac{N}{\lambda}\right)^{\kappa}\right]. \tag{4}$$

The dependence of the fatigue life distribution on the applied stress amplitude, σ_a, is embedded in the scale parameter, λ, by

$$\ln(\lambda) = \gamma_0 + \gamma_1 \ln(\sigma_a), \tag{5}$$

where γ_0 and γ_1 are constants. Eq. (5) is chosen to use because it essentially has the same as the natural logarithm of the Basquin model, which classically describes the relationship between the fatigue life and stress amplitude [59].

Eqs. (3) and (4), when combining with Eq. (5), can then describe the probability distribution and cumulative distribution of the experimental fatigue data (σ_a, N), with κ, γ_0, and γ_1 being three unknown parameters. κ, γ_0, and γ_1 can be estimated by the maximum likelihood method [39,52], i.e., maximize the following likelihood function

$$L(\kappa,\ \gamma_0, \gamma_1) = \prod_{i=1}^{n} \left\{ \left[\frac{\kappa}{\lambda(\sigma_a^i)} \left(\frac{N_i}{\lambda(\sigma_a^i)} \right)^{\kappa-1} \right]^{\delta_i} \cdot \exp\left[-\left(\frac{N_i}{\lambda(\sigma_a^i)} \right)^{\kappa} \right] \right\}, \tag{6}$$

with $\lambda(\sigma_a^i) = \exp[\gamma_0 + \gamma_1 \ln(\sigma_a^i)]$ according to Eq. (5). n is the total number of fatigue data points. σ_a^i and N_i are the stress amplitude and fatigue life of the ith sample, respectively. Herein δ_i is a censoring indicator. $\delta_i = 1$ if the ith sample fractured by 10^7 cycles, while $\delta_0 = 0$ if the ith sample had not fractured when 10^7 cycles were reached. With the maximum likelihood method, κ, γ_0, and γ_1 are determined to be 0.59, 825.35, and 130.31, respectively, for the fatigue data of the HfNbTaTiZr.

With the known κ, γ_0, and γ_1, the fatigue life of the HfNbTaTiZr at a given stress amplitude can be predicted by the p quantile life. The quantile function is derived by finding the value of N_p for which $F(N_p;\ \lambda, \kappa) = p$. Mathematical derivation finally gives

$$N_p = [-\ln(1-p)]^{1/\kappa} \cdot \exp[\gamma_0 + \gamma_1 \ln(\sigma_a)], \tag{7}$$

The median quartile at $p = 0.5$, i.e., $N_{0.5}$, can be used to estimate the average fatigue life as a function of the stress amplitude, as given by the solid curve in Fig. 4(b). The quartiles at $p = 0.025$ and $p = 0.975$, i.e., $N_{0.025}$ and $N_{0.975}$, are employed to construct the 95% predictive interval, as given by the red/blue curves in Fig. 4(b). Overall, the 2-parameter Weibull model can well describe the fatigue life distribution of the HfNbTaTiZr in a wide range of applied stress amplitudes. The fatigue strength, σ_{af}, is estimated by solving Eq. (7) at $N_p = 1 \times 10^7$ and $p = 0.5$ for σ_a, which ultimately gives 495.42 MPa with a 95% predictive interval of (474.61,

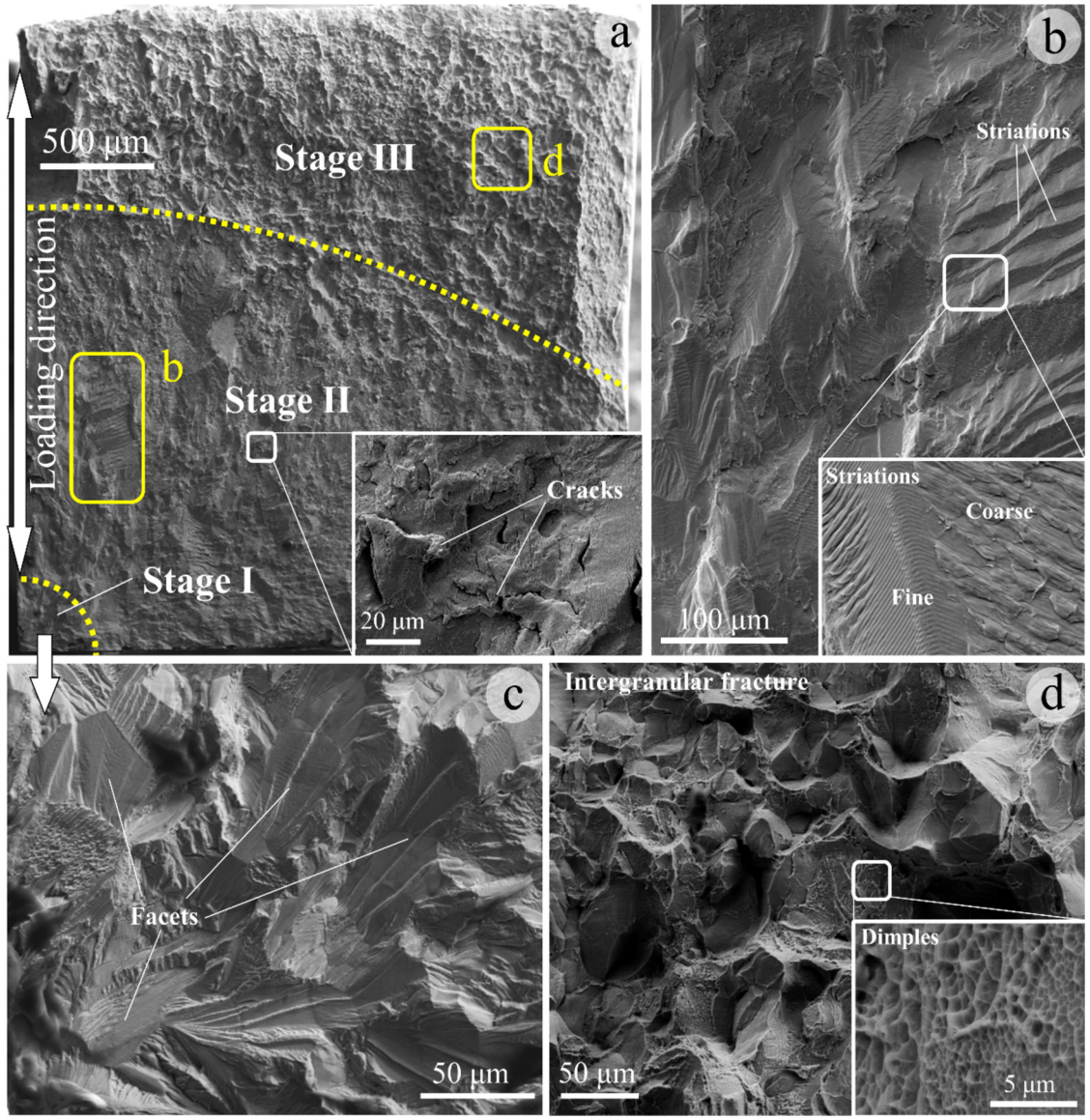

Fig. 9. Fracture surface morphologies of the sample fatigue-failed at $\sigma_{max} = 1123$ MPa and $N_f = 148868$. (a) Overall view. Magnified views of (b) region b in stage II, (c) stage I, and (d) region d in stage III.

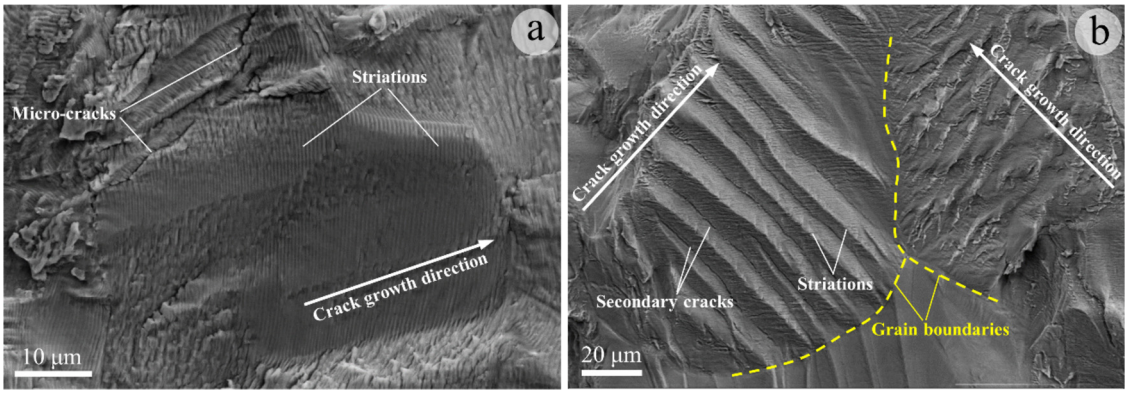

Fig. 10. Magnified fracture-surface morphologies in stage II, showing (a) fine striations with secondary cracks across striations and (b) coarse striations with secondary cracks between striations. The sample failed at $\sigma_{max} = 1179$ MPa and $N_f = 23395$.

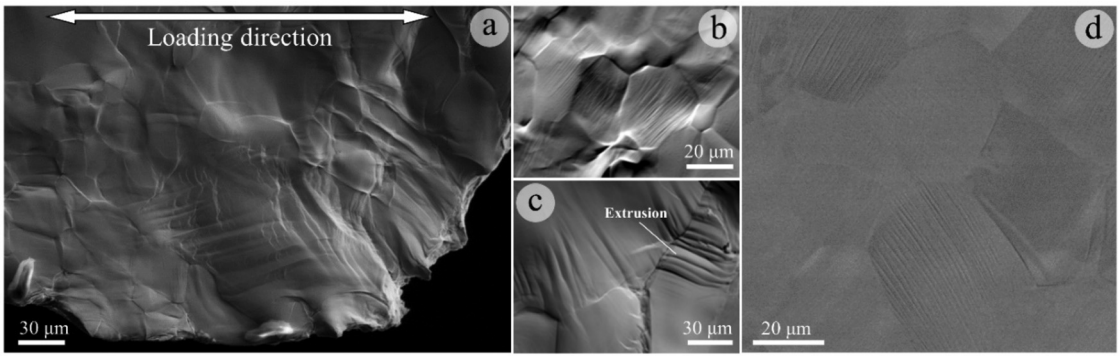

Fig. 11. SEM images of plastic deformation in the vicinity of the main fatigue crack, the sample failed at $\sigma_{max} = 1119$ MPa and $N_f = 107553$. (a) Overview. (b) Highly strained grains with a high density of slip lines. (c) Grains with extrusions from persistent slip bands. (d) The region somewhat away from the crack, still showing dense slip lines in grains.

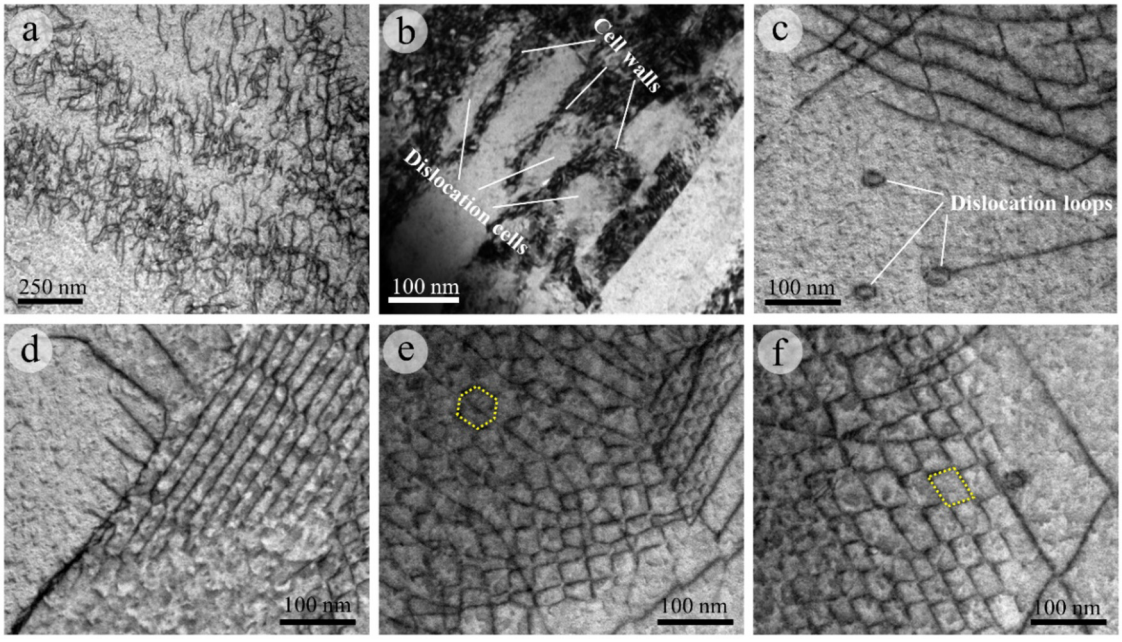

Fig. 12. Bright-field STEM/TEM images in the vicinity of the main fatigue crack, showing various dislocation substructures. (a) Dislocation tangles. (b) Dislocation cells separated by walls. (c) Dislocation loops. (d) Dislocation arrays. (e) Dislocation network composed predominantly of hexagonal cells. (f) The dislocation network consisted predominantly of parallelogrammatic cells. The TEM image in (b) was taken with $g = \{110\}$ and zone axis $\approx \langle 001 \rangle$, whereas the STEM images in the remaining sub-graphs were obtained with $g = \{10\bar{1}\}$ and zone axis $\approx \langle 111 \rangle$, all under a two-beam condition. The sample for (b) failed at $\sigma_{max} = 1149$ MPa and $N_f = 275729$, while the rest at $\sigma_{max} = 1139$ MPa and $N_f = 34041$.

506.28 MPa). The Weibull model decently catches the experimental fatigue strength of 497 MPa. Accordingly, the Weibull model can faithfully capture the probabilistic nature of the fatigue data and is a useful tool to predict the fatigue life of the HfNbTaTiZr HEA in a statistical sense.

5. Discussion

5.1. Comparison of fatigue resistance

As the high-cycle fatigue data of a dozen of HEAs with different compositions and microstructures are available from the literature [60], it is intriguing to compare the current bcc HEA with those investigated already in terms of their fatigue performance. The comparison of fatigue strengths is made in Fig. 14(a). For a fair comparison, all fatigue data are converted to be at $R = -1$ with [60]

$$\sigma_{a,1} = \sigma_{a,2}\sqrt{\frac{1-R_1}{1-R_2}}, \tag{8}$$

where $\sigma_{a,1}$ and $\sigma_{a,2}$ are the stress amplitudes at the stress ratios of R_1 and R_2, respectively. Eq. (8) is derived from the Smith–Watson–Topper relation between the fatigue quantities obtained at different stress ratios, i.e., $\sigma_{max,1}\sigma_{a,1} = \sigma_{max,2}\sigma_{a,2}$, where the subscripts 1 and 2 represent the data at the stress ratios of R_1 and R_2, respectively [61].

Based on phase structures, all HEAs in the $\sigma_{af} - \sigma_{UTS}$ map of Fig. 14(a) are classified into three groups. They are (1) the fcc HEAs with low fatigue and tensile strengths; (2) the multi-phase HEAs with moderate fatigue and tensile strengths; (3) the bcc HfNbTaTiZr HEA with high fatigue strength yet moderate tensile strength. Clearly, the fatigue strength of the HfNbTaTiZr exceeds all HEAs with known high-cycle fatigue data.

Considering that the HfNbTaTiZr is a concentrated bcc alloy, it is also interesting to compare its fatigue performance with that of its dilute counterparts [62]. It is noted from Fig. 14(a) the dilute bcc alloys are located on the bottom-left corner, signaling both drastically lower fatigue and tensile strengths than the HfNbTaTiZr alloy. It seems that the pronounced solid-solution strength-

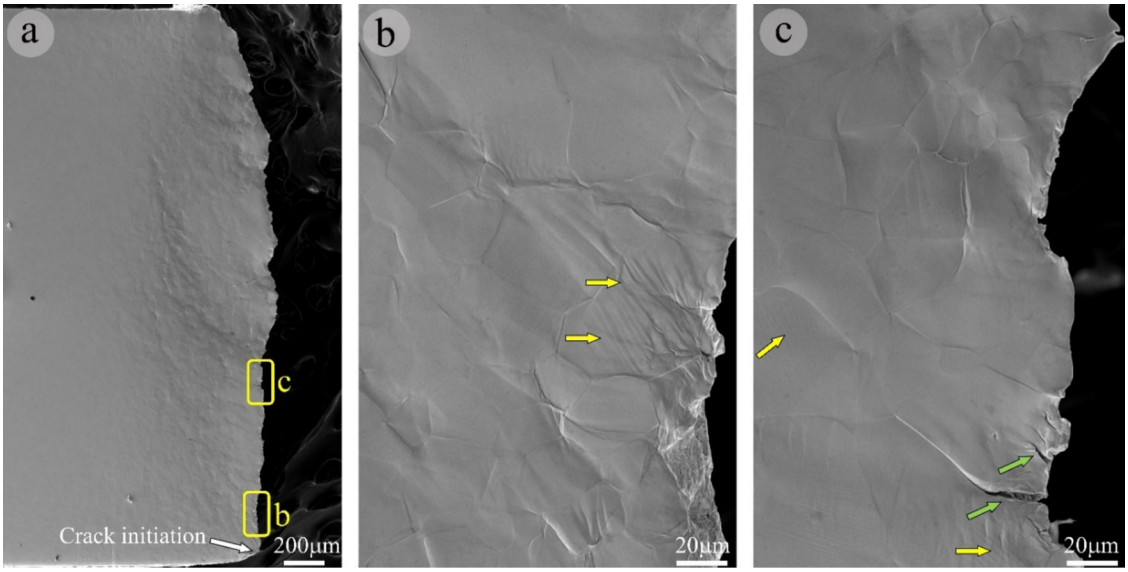

Fig. 13. SEM images of plastic deformation in the vicinity of the main fatigue crack, the sample failed at $\sigma_{max} = 1114$ MPa and $N_f = 2200000$. (a) Overview. (b) Highly strained grains with extrusions from persistent slip bands. (c) Secondary cracks with dense slip lines.

ening in HEAs improves not only uniaxial strength but also fatigue strength.

A more extensive comparison involves conventional alloys for common structural applications, i.e., steels, titanium alloys, aluminum alloys, and magnesium alloys [60]. This comparison can facilitate our understanding about the potential of the HfNbTaTiZr alloy in fatigue-resistant applications. From Fig. 14(a), it is seen that the fatigue strength of the HfNbTaTiZr lies on the upper end of that of conventional alloys with similar tensile strength. It suggests that the bcc HfNbTaTiZr possesses fairly promising fatigue resistance.

In a similar fashion, the fatigue ratio of the HfNbTaTiZr alloy exceeds that of all other HEAs with reported high-cycle fatigue data, dilute bcc alloys, and the vast majority of conventional alloys but some medium-strength steels, as evidenced in Fig. 14(b).

5.2. Low-cycle fatigue mechanisms

The analyses of crack propagation trajectories and fracture surface morphologies indicate that a number of extrinsic toughening mechanisms are available in the HfNbTaTiZr HEA to shield the crack tip, causing the increased resistance to fatigue-crack propagation. The observed extrinsic toughening mechanisms include the crack deflection and meandering, fracture-debris-induced crack closure, roughness-induced crack closure (or crack interlocking), and crack branching, which all act in the crack wake as schematically illustrated on the left side of Fig. 15. These extrinsic toughening mechanisms are not all independent of each other. Rather, one may accompany another. For example, frequent crack deflection can induce roughness-induced crack closure [e.g., Fig. 7(a)], crack branching and deflection can cause fracture-debris-induced crack closure [e.g., Fig. 7(c)], and crack branching may come with crack deflection and meandering [e.g., Fig. 6]. These extrinsic toughening mechanisms act at the wake of the crack tip to reinforce the fatigue resistance of the present alloy, as in many other materials [50,51,63,64].

In principle, fatigue-crack extension in a material is driven by the globally applied stress intensity factor range, $\Delta K = K_{max} - K_{min}$, where K_{max} and K_{min} are the maximum and minimum applied stress intensity factors derivable from the maximum and minimum applied stresses, σ_{max} and σ_{min} [19]. For the idealized mode-I crack propagation without any crack-tip shielding, the global characterizing parameter, ΔK, can neatly quantify the driving force of fatigue-crack growth [19]. Nevertheless, once extrinsic toughening is present, the local driving force experienced at the crack tip turns to differ from the global ΔK. In fact, extrinsic shielding causes an extra stress intensity K_s, which negatively contributes to the global driving force, ΔK, to result in a reduced near-tip stress intensity factor range, i.e., $\Delta K_{tip} = \Delta K - K_s$ [51]. Since the fatigue-crack-growth rate, $\frac{da}{dN}$, has a power-law dependence on the stress intensity factor range, ΔK, according to the Paris' law of $\frac{da}{dN} = C\Delta K^m$, where C and m are constants [19], the reduction of ΔK to ΔK_{tip} at the crack tip by any form of extrinsic toughening is expected to significantly decelerate the fatigue-crack-growth rate. For the HfNbTaTiZr HEA under investigation, all four extrinsic toughening mechanisms identified are anticipated to retard fatigue crack extension, though in distinct manners, as will be discussed individually in the following.

Crack deflection and meandering: Crack deflection and meandering can turn a mode-I fracture into a mixed-mode fracture through the deviation of the crack propagation path from the plane normal to the remote stress. It leads to the decomposition of the original model-I stress intensity into local mode-I and mode-II stress intensities [65]. Since the local mode-I stress intensity at deviated cracks is reduced relative to the original model I stress intensity, crack growth rates are diminished.

The degree of crack retardation by crack deflection is first dictated by the kink angle, which determines the portions of the decomposed mode-I and II stress intensities. Besides, the length of the deflected crack segment is also critical as it determines the extent of cracks that have experienced a reduced stress intensity. By considering the combined effect from the kink angle, θ, and the deflected crack length, b, along with the undeflected crack length, c, the changes in the stress intensity, ΔK_{tip}, and the fatigue-crack-growth rate, $(\frac{da}{dN})_{tip}$, at the crack tip are given as [51,66]

$$\Delta K_{tip} = \frac{b\cos^2(\theta/2) + c}{b + c}\Delta K, \tag{9}$$

$$\left(\frac{da}{dN}\right)_{tip} = \frac{b\cos\theta + c}{b + c}\frac{da}{dN}, \tag{10}$$

where ΔK and $\frac{da}{dN}$ are the stress intensity and fatigue-crack-growth rate in the absence of crack deflection.

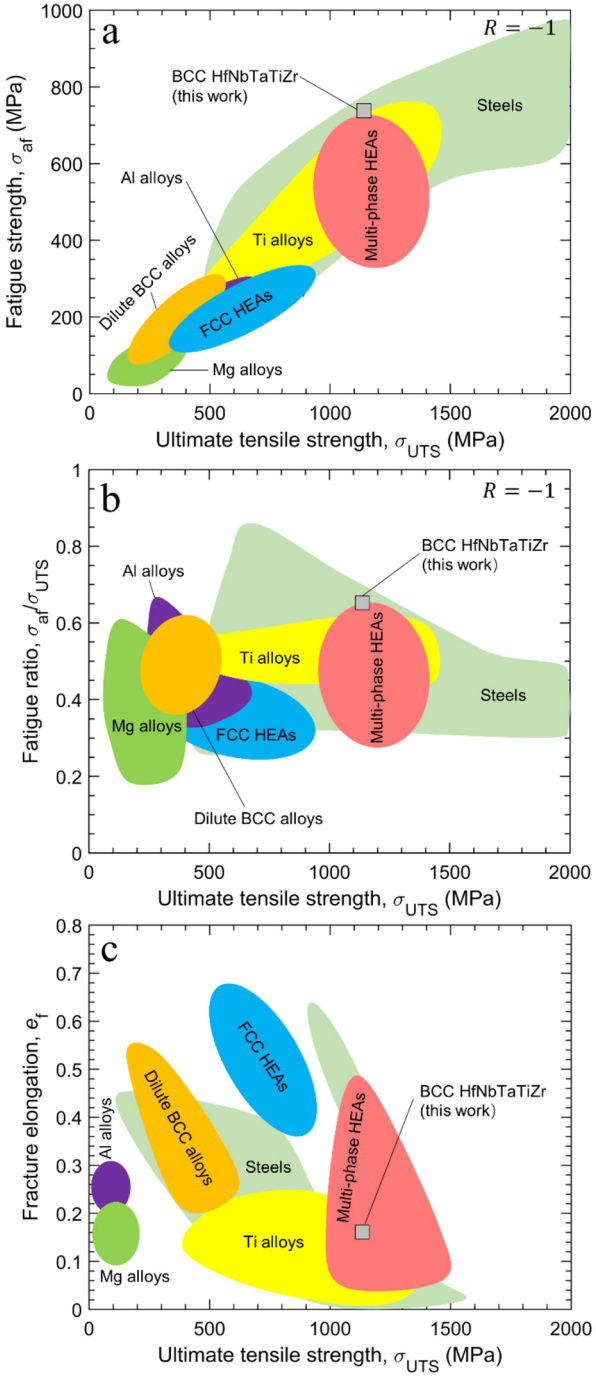

Fig. 14. Comparison of the fatigue properties of the HfNbTaTiZr alloy with other high-entropy and conventional alloys. (a) Fatigue strength and (b) fatigue ratio versus ultimate tensile strength. All fatigue data are converted to be at $R = -1$ with the Smith–Watson–Topper relation [61]. (c) Fracture elongation versus ultimate tensile strength. The data for all other alloys are taken from Refs. [60,62,80,81]. Note that steels with tensile strength greater than 2000 MPa are not included in (a) and (b), greater than 1600 MPa not in (c).

Now consider the two consecutively defected cracks in Fig. 5(a). The first deflected crack has $b \approx 2071.40$ μm, $c \approx 500$ μm, and $\theta \approx 40°$; With Eqs. (9) and (10), $\frac{\Delta K_{tip}}{\Delta K}$ and $(\frac{da}{dN})_{tip}/\frac{da}{dN}$ are calculated to be 0.91 and 0.81. This means that, by this crack deflection, the near-tip driving force for crack extension is reduced by ~9% whereas the fatigue-crack-growth rate is lowered by ~19% (greater reduction due to its power law dependence on ΔK). For the second deflected crack, $b \approx 571.40$ μm, $c \approx 428.60$ μm, and $\theta \approx 90°$, and $\frac{\Delta K_{tip}}{\Delta K}$ and $(\frac{da}{dN})_{tip}/\frac{da}{dN}$ are calculated to be 0.71 and 0.42. Therefore, ΔK_{tip} is reduced by ~29% relative to ΔK whereas $(\frac{da}{dN})_{tip}$ is reduced by ~58% relative to $\frac{da}{dN}$. From these quantitative calculations, it is clear that crack deflection can effectively retard the propagation of fatigue cracks. The same also happens to crack deflection observed in Figs. 6, 7(a) and 8. Generally, crack deflection and meandering in retarding the propagation of fatigue cracks becomes more significant with the increase in its extent, the kink angle, and the length of deflected crack segments.

Roughness-induced crack closure: Frequent crack deflection tends to create torturous or serrated crack propagation paths (e.g., Figs. 7 and 8), which can impose two important effects on fatigue-crack propagation. First, it creates high fracture surface asperities. Second, it induces a locally mixed-mode fracture. The shear component in the mixed-mode fracture displaces the crack flanks oppositely in the direction parallel to the crack path, which can lead to the closure of serrated cracks upon unloading. The crack closure induced by these two effects does not cease until the crack-tip-opening displacement (CTOD) in the new cycle of loading becomes large enough to disengage two interlocked crack flanks. During this process, the global stress intensity factor range, $\Delta K = K_{max} - K_{min}$, is reduced to $\Delta K_{tip} = K_{max} - K_{cl}$ at the crack tip, where K_{cl} is the closure stress intensity factor greater than K_{min} but smaller than K_{max}. So, through the roughness-induced crack closure, the near-tip driving force of crack extension is diminished and crack propagation is arrested.

The near-tip driving force of fatigue-crack extension, ΔK_{tip}, decreases with increasing K_{cl}. The magnitude of K_{cl} relies on both the roughness of crack surfaces and the extent of the mode-II shearing displacement at the crack tip. With the aid of a simple geometry model, K_{cl} upon the first asperity contact is estimated to be [67]

$$K_{cl} \approx K_{max}\left(\frac{2\gamma X}{1+2\gamma X}\right)^{1/2}, \tag{11}$$

where γ is the fracture surface roughness defined as the ratio of the height to the width of asperities, X is the ratio of the mode-II to mode-I displacements at the crack tip. Taking the serrated crack closure in Fig. 7(a) as an example, the average fracture surface roughness over all apparent crack serrations, γ_{mean}, is estimated to be 0.45. By simply treating X as $\tan(\theta)$, where θ is the kink angle at each individual crack deflection, the average mode-II to mode-I ratio, X_{mean}, is calculated to be 0.53. Substituting the values of γ and X into Eq. (11), we determine $K_{cl} \approx 0.57K_{max}$. This feature gives rise to $\Delta K_{tip} = K_{max} - 0.57K_{max} = 0.43K_{max}$, much smaller than the global stress intensity range, $\Delta K = K_{max} - 0.1K_{min} = 0.9K_{max}$. Similarly, for the crack interlocking induced by intergranular fracture in Fig. 8, $\gamma_{mean} = 0.44$, and $X_{mean} = 0.65$, resulting in $K_{cl} \approx 0.6K_{max}$. Also for the serrated crack closure in Fig. 5(c), $\gamma_{mean} = 0.48$, and $X_{mean} = 1.04$, leading to $K_{cl} \approx 0.71K_{max}$. Accordingly, the roughness-induced fatigue crack closure can apparently reduce the fatigue-crack-growth rate by lifting K_{min} up to K_{cl}.

The retardation of crack propagation by the roughness-induced crack closure is believed to be most effective at low stress intensity factor ranges, where the size-scale of the fracture-surface roughness is comparable to CTODs [51]. Its effectiveness in reducing near-threshold crack growth rates or increasing the threshold stress intensity factor range, ΔK_{th}, has been demonstrated in many alloys systems, such as pearlitic eutectoid steel [68], 7475 aluminum alloy [69], and low-carbon steel with duplex ferritic-martensitic microstructures [70].

Fracture-debris-induced crack closure: The oxide- or corrosion-debris-induced crack closure is a shielding mechanism mostly effective at low stress intensity factor ranges, analogous to the

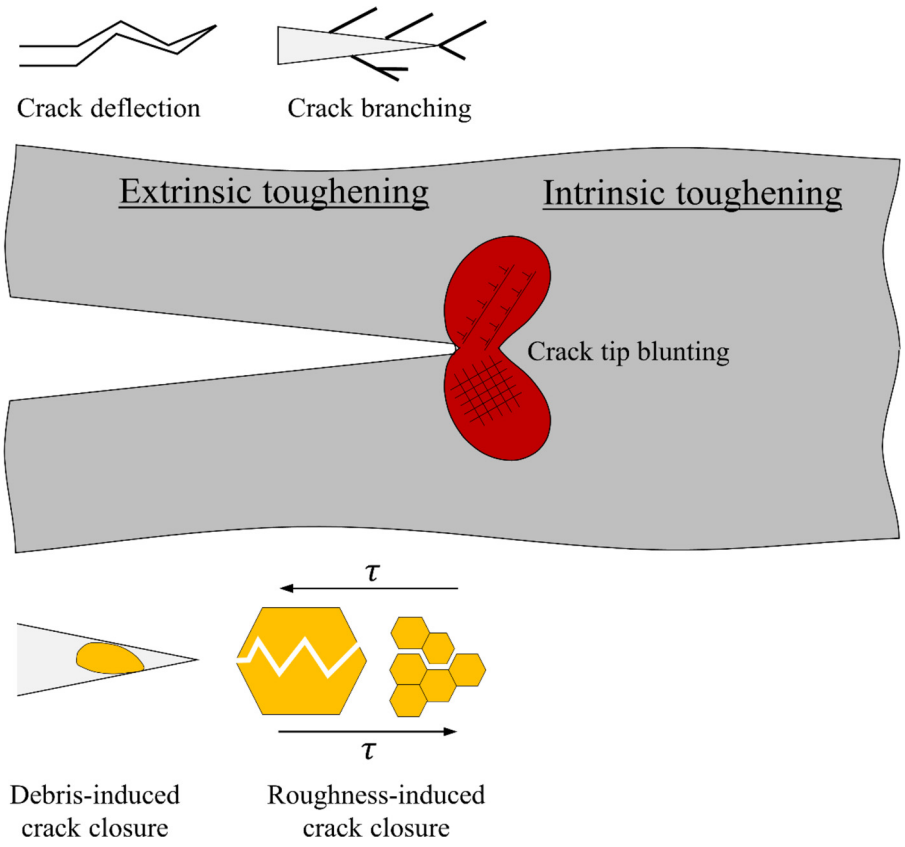

Fig. 15. Schematic depicting the intrinsic and extrinsic toughening mechanisms observed in the HfNbTaTiZr alloy.

roughness-induced crack closure [51]. This extrinsic toughening mechanism is triggered by the mechanical wedging action of insoluble corrosion products deposited at the crack wake, notably in the corrosion fatigue of metallic materials [48,49]. Likewise, this mechanism can raise the minimum stress intensity at the crack tip from the global value K_{min} to the closure stress intensity K_{cl}, thus reducing the local near-tip stress intensity range from $\Delta K = K_{max} - K_{min}$ to $\Delta K_{tip} = K_{max} - K_{cl}$. As $\Delta K_{tip} < \Delta K$, the crack extension is effectively retarded. The slower near-threshold fatigue crack growth rates of structural steels in water or steam than in air is a good demonstration of the effectiveness of this extrinsic toughening mechanism [71].

In our case of fatigue in air, shielding debris does not originate from corrosion or oxidation on crack surfaces. Instead, it is a result of crack branching and remerging following deflection, as representatively shown in Fig. 7(c). We, therefore, name this shielding mechanism as fracture-debris-induced crack closure. From Fig. 7(c), it is expected that the fracture debris would have a similar wedging effect to oxides or corrosion debris in retarding crack extension. When the crack surfaces come into contact upon unloading, by considering the debris as a rigid wedge the closure stress intensity at the crack tip is estimated to be [51]

$$K_R = \frac{sE}{4\left(1-\nu^2\right)\left(\frac{\pi l}{2}\right)^{1/2}}, \tag{12}$$

where E is Young's modulus, ν is Poisson's ratio, s is the thickness of the wedge, l is the distance from the crack tip to the wedge. From Eq. (12), it is obvious that the closer the debris is to the crack tip, the more reduction it can bring to the stress intensity factor range. The debris in the immediate vicinity of the crack tip has the most dominating effect. Also, the thicker the debris the greater the reduction in the stress intensity range. The debris in Fig. 7(c) has $l \approx 7.0\ \mu$m and $s \approx 6.6\ \mu$m. Similar to the toughness-induced crack closure, the fracture-debris-induced crack closure maximize its effects when the size of debris is comparable to CTOD.

Crack branching: Crack branching in toughening a material is relatively easy to comprehend. According to Irwin's energy approach for fracture [47,72], the energy release rate that drives an increment of crack extension is given as $G = -\frac{d\Pi}{dA} = \frac{-(dU-dV)}{dA}$, where Π is the potential energy equal to the difference between the strain energy stored in the body, U, and the work done by external forces, V, A is the area of crack surfaces. By crack branching, at the same level of decrease in the potential energy, $d\Pi$, the increment in the crack-surface area, dA, becomes greater in comparison to the case without crack branching. In other words, the same amount of potential energy is dissipated into a greater area of fracture surfaces. The energy release rate, G, therefore, decreases to slow down crack-extension rates. Crack branching in improving fatigue resistance has been reported in a wide variety of material systems [73–76]. Widespread crack branching at different scales is observed as well in the present alloy to delay its fatigue failure (e.g., Figs. 5 and 7). More importantly, certain crack branching, e.g., that in Fig. 7(b), manifests a hierarchical character, i.e., tertiary or higher-order cracks form from the branching of secondary cracks. The hierarchy in crack branching can lead to tree-like crack path patterns to maximize the dissipation of the potential energy and thus the retardation of the propagation of the major crack.

Microscopically, crack branching and induced secondary cracks are likely to stem from cleavage cracking on {100} planes when sessile dislocations are created by Cottrell reactions of $\frac{a}{2}[1\bar{1}1] + \frac{a}{2}[11\bar{1}] \rightarrow a[100]$ type, with <111> dislocations gliding on {110} planes.

5.3. High-cycle fatigue mechanisms

It is known that stronger materials resist crack initiation better. In light of this wisdom, the high fatigue strength of the HfNbTaTiZr alloy is ascribed to its high tensile strength. From the microstructural perspective, cracks in metals frequently initiate from inclusions or surface extrusions and intrusions produced when persistent slip bands (PSBs) come to meet free surfaces. The more localized the PSBs are, the quicker the crack initiates. Fig. 13 signals that crack initiation in the present alloy commences on the surface, arguably by extrusions and intrusions of PSBs. Observing the microstructural characteristics at the vicinity of crack initiation site, no obvious localized PSBs is noticed. Instead, slip lines well spread out within grains. The outspreading of slip lines retards the formation of PSBs, and thus crack initiation. Accordingly, a high fatigue strength is anticipated.

5.4. Deformation mechanisms

The microstructural examinations in the near-crack region in Section 3.3.3 indicate a large extent of plastic deformation accommodated by extensive dislocation activities. The large plasticity in a wide range of strain levels can constantly retard both crack initiation and crack propagation. According to a classic phenomenological model by Laird and Smith [77], fatigue-crack growth in stage II is accomplished by a repetitive process of plastic blunting and sharpening of crack tips under the action of alternate tensile and compressive loads. From the fracture mechanics standpoint, the considerable plasticity in a large plastic zone repeatedly blunts crack tips, thereby effectively arresting crack propagation. The pronounced plasticity ahead of crack tips serves as an intrinsic source to toughen the alloy and keep its fatigue resistance high. The intrinsic toughening mediated through large-scale dislocation activities, as schematically described in Fig. 15, is inherent to the HfNbTaTiZr alloy and thus are active irrespective of crack size and location.

The plastic deformation of concentrated bcc HEAs have been reported to be drastically distinct from their dilute counterparts, as a direct result of their inherently large lattice distortion and local chemical fluctuation (or short-range order) [78,79]. In a recent study of the bcc HfNbTiZr [79], it was proven by *in-situ* TEM observations that local chemical fluctuation (LCF) induced large lattice strain can pin mobile dislocations. Different from brittleness resulting from "kink pair" induced pinning in dilute bcc alloys, LCF-induced pinning in the bcc HEA is beneficial to ductility in addition to the strengthening effect. This is because it constantly leaves tons of dislocation loops behind as deformation proceeds. These dislocation loops act as steady sources of dislocation multiplication via enlargement and impingement with other moving dislocations. LCF also induces a rugged energy landscape in HEAs [78,79], causing rugged dislocation motion and thus local double cross-slips. Local double cross-slip is a ponent mechanism that can distribute dislocation-multiplication over a variety of planes, thus alleviating strain location and retarding crack nucleation. The HfNbTaTiZr herein is chemically like the HfNbTiZr, and therefore, analogous micro-deformation mechanisms are expected to transpire. Without delicate *in-situ* TEM observations, the analogy in micro-deformation of the present alloy is in part evidenced from the appearance of many dislocation loops (e.g., Fig. 12(a) and (f)) and wavy dislocation traces (implying cross-slips, e.g., Fig. 12(a)–(c), and (e)).

These atomic scale micro-mechanisms are fundamental reasons for exceptional fatigue resistance of the HfNbTaTiZr HEA. The link between these micro-mechanisms and intrinsic toughening is already elaborated above. These micro-mechanisms are also expected to contribute to the simultaneous occurrence of multiple extrinsic toughening mechanisms discussed heretofore. At first, LCF creates a heterogeneous atomic environment, in which atomic bonds vary in strength from location to location. As a crack propagates, it is inclined to pick the weakest bond in the neighborhood to break up. Accordingly, frequent crack deflection and meandering results. If several bonds with similar strengths co-exist ahead of a crack tip, the crack may end up rupturing multiple bonds at the same time, resulting in crack branching. Crack closure, on the other hand, is a derivative of crack meandering and branching. Overall, intrinsic toughening accounts primarily for excellent fatigue resistance of the HfNbTaTiZr alloy whereas extrinsic toughening is secondary, given the fact that ~90% of high-cycle fatigue life in metals is consumed by crack initiation.

6. Conclusions

The present work reports that the cold-rolled and annealed HfNbTaTiZr alloy has a yield strength of 1113 ± 48 MPa, an ultimate tensile yield strength of 1139 ± 42 MPa and a total elongation of 0.16 ± 0.016. Nevertheless, a deep analysis of the necking point indicates that a large portion of tensile ductility is attributed to strain softening while strain hardening engages only up to an engineering strain of 0.048.

The fatigue properties along with associated fatigue mechanisms of the alloy are particularly investigated in depth, from which the following crucial conclusions are drawn.

(1) The HfNbTaTiZr alloy is tested to have a fatigue strength of 497 MPa and a fatigue ratio of 0.44 at a frequency of $f = 10$ Hz and a stress ratio of $R = 0.1$. With the Smith–Watson–Topper relation [61], the fatigue strength and fatigue ratio of the alloy at $R = -1$ are estimated to be 741 MPa and 0.65, respectively. The fatigue resistance of the HfNbTaTiZr exceeds that of all other high-entropy alloys with reported high-cycle fatigue data, dilute bcc alloys, and many structural alloys such as steels, titanium alloys, and aluminum alloys.
(2) In the high-cycle regime, the remarkable fatigue resistance is macroscopically ascribed to the alloy's high strength, and microscopically to delayed crack initiation by detaining the formation of localized persistent slip bands (PSBs).
(3) In the low-cycle regime, resistance to fatigue crack growth is accomplished primarily by intrinsic toughening, which is fulfilled by dislocation-mediated crack-tip blunting at crack tips, and secondarily by extrinsic toughening, which is empowered by several mechanisms in one place such as by crack deflection and meandering, fracture-debris-induced crack closure, roughness-induced crack closure, and crack branching.
(4) The Weibull predictive model can faithfully capture the probabilistic nature of the high-cycle fatigue data and is a useful tool to predict the fatigue life of the HfNbTaTiZr HEA.

The conclusions drawn are critical to making intelligent assessments on the qualification of refractory HEAs in practical engineering applications.

Acknowledgements

The authors thank the support of the Department of Energy (DOE) Office of Fossil Energy, National Energy Technology Laboratory (NETL) (DE-FE-0011194), the National Science Foundation (DMR1611180 and 1809640), and the U.S. Army Office Projects (W911NF-13-1-0438 and W911NF-19-2-0049) with Drs. J. Mullen, V. Cedro, R. Dunst, S. Markovich, J. Yang, G. Shiflet, D. Farkas, M. P. Bakas, D. M. Stepp, and S. Mathaudhu as program managers. S.Y.C. acknowledges the financial support from the National Natural Science Foundation of China (No. 52001271), and the Shandong Major Scientific and Technological Innovation Program, China

(No. 2019JZZY010325). S.Y.C. and P.K.L. would like to acknowledge the financial support of the Center for Materials Processing (CMP), at The University of Tennessee, with the director of Dr. Claudia J. Rawn. J.W.

References

[1] W. Li, D. Xie, D. Li, Y. Zhang, Y. Gao, P.K. Liaw, Prog. Mater. Sci. 118 (2021) 100777.
[2] J.W. Yeh, S.K. Chen, S.J. Lin, J.Y. Gan, T.S. Chin, T.T. Shun, C.H. Tsau, S.Y. Chang, Adv. Eng. Mater. 6 (2004) 299–303.
[3] F. Otto, Y. Yang, H. Bei, E.P. George, Acta Mater. 61 (2013) 2628–2638.
[4] E.P. George, D. Raabe, R.O. Ritchie, Nat. Rev. Mater. 4 (2019) 515–534.
[5] Z. Li, K.G. Pradeep, Y. Deng, D. Raabe, C.C. Tasan, Nature 534 (2016) 227–230.
[6] W. Li, P.K. Liaw, Y. Gao, Intermetallics 99 (2018) 69–83.
[7] O.N. Senkov, G.B. Wilks, D.B. Miracle, C.P. Chuang, P.K. Liaw, Intermetallics 18 (2010) 1758–1765.
[8] S. Chen, W. Li, X. Xie, J. Brechtl, B. Chen, P. Li, G. Zhao, F. Yang, J. Qiao, P.K. Liaw, J. Alloy. Compd. 752 (2018) 464–475.
[9] D.H. Lee, M.Y. Seok, Y. Zhao, I.C. Choi, J. He, Z. Lu, J.Y. Suh, U. Ramamurty, M. Kawasaki, T.G. Langdon, J.I. Jang, Acta Mater. 109 (2016) 314–322.
[10] W. Li, G. Wang, S. Wu, P.K. Liaw, J. Mater. Res. 33 (19) (2018) 3011–3034.
[11] P. Chen, C. Lee, S.Y. Wang, M. Seifi, J.J. Lewandowski, K.A. Dahmen, H. Jia, X. Xie, B. Chen, J.W. Yeh, C.W. Tsai, T. Yuan, P.K. Liaw, Sci. China Technol. Sci. 61 (2018) 168–178.
[12] S.Y. Chen, L. Wang, W.D. Li, Y. Tong, K.K. Tseng, C.W. Tsai, J.W. Yeh, Y. Ren, W. Guo, J.D. Poplawsky, P.K. Liaw, Mater. Res. Lett. 7 (2019) 475–481.
[13] F. Otto, A. Dlouhý, C. Somsen, H. Bei, G. Eggeler, E.P. George, Acta Mater. 61 (2013) 5743–5755.
[14] Z. Wu, H. Bei, G.M. Pharr, E.P. George, Materialia 81 (2014) 428–441.
[15] A. Gali, E.P. George, Intermetallics 39 (2013) 74–78.
[16] B.D. Miracle, D.J. Miller, N.O. Senkov, C. Woodward, D.M. Uchic, J. Tiley, Entropy 16 (2014) 494–525.
[17] C. Zhang, M. Gao, J. Yeh, P. Liaw, Y. Zhang, High-Entropy Alloys: Fundamentals and Applications, Springer, Berlin, Germany, 2016.
[18] P. Sathiyamoorthi, H. Kim, Adv. Eng. Mater. 20 (2017) 1700645.
[19] S. Suresh, Fatigue of Materials, Cambridge University Press, Cambridge, 1998.
[20] F. Bahadur, K. Biswas, N.P. Gurao, Int. J. Fatigue 130 (2020) 105258.
[21] Z. Li, K.G. Pradeep, Y. Deng, D. Raabe, C.C. Tasan, Nature 534 (2016) 227.
[22] Z. Chlup, S. Fintová, H. Hadraba, I. Kuběna, M. Vilémová, J. Matějíček, Metals 9 (2019) 1110.
[23] Y.Z. Tian, S.J. Sun, H.R. Lin, Z.F. Zhang, J. Mater. Sci. Technol. 35 (2019) 334–340.
[24] K. Suzuki, M. Koyama, H. Noguchi, Procedia Struct. Integr. 13 (2018) 1065–1070.
[25] K. Suzuki, M. Koyama, S. Hamada, K. Tsuzaki, H. Noguchi, Int. J. Fatigue 133 (2020) 105418.
[26] N. Kashaev, V. Ventzke, N. Petrov, M. Horstmann, S. Zherebtsov, D. Shaysultanov, V. Sanin, N. Stepanov, Mater. Sci. Eng. A 766 (2019) 138358.
[27] Y.K. Kim, G.S. Ham, H.S. Kim, K.A. Lee, Intermetallics 111 (2019) 106486.
[28] K. Liu, S.S. Nene, M. Frank, S. Sinha, R.S. Mishra, Mater. Res. Lett. 6 (11) (2018) 613–619.
[29] K. Liu, S.S. Nene, M. Frank, S. Sinha, R.S. Mishra, Appl. Mater. Today 15 (2019) 525–530.
[30] S. Shukla, T. Wang, S. Cotton, R.S. Mishra, Scr. Mater. 156 (2018) 105–109.
[31] K. Liu, M. Komarasamy, B. Gwalani, S. Shukla, R.S. Mishra, Scr. Mater. 158 (2019) 116–120.
[32] K. Liu, B. Gwalani, M. Komarasamy, S. Shukla, T. Wang, R.S. Mishra, Mater. Sci. Eng. A 760 (2019) 225–230.
[33] K.V.S. Thurston, B. Gludovatz, Q. Yu, G. Laplanche, E.P. George, R.O. Ritchie, J. Alloy. Compd. 794 (2019) 525–533.
[34] K.V.S. Thurston, B. Gludovatz, A. Hohenwarter, G. Laplanche, E.P. George, R.O. Ritchie, Intermetallics 88 (2017) 65–72.
[35] W. Li, X. Long, S. Huang, Q. Fang, C. Jiang, Eng. Fract. Mech. 218 (2019) 106579.
[36] B. Guennec, V. Kentheswaran, L. Perrière, A. Ueno, I. Guillot, J.P. Couzinié, G. Dirras, Intermetallics 110 (2019) 106459.
[37] T. Eguchi, M. Koyama, Y. Fukushima, C.C. Tasan, K. Tsuzaki, Proc. Struct. Integr. 13 (2018) 831–836.
[38] M. Seifi, D. Li, Z. Yong, P.K. Liaw, J.J. Lewandowski, JOM 67 (2015) 2288–2295.
[39] M.A. Hemphill, T. Yuan, G.Y. Wang, J.W. Yeh, C.W. Tsai, A. Chuang, P.K. Liaw, Materialia 60 (2012) 5723–5734.
[40] Z. Tang, T. Yuan, C.W. Tsai, J.W. Yeh, C.D. Lundin, P.K. Liaw, Acta Mater. 99 (2015) 247–258.
[41] B. Guennec, V. Kentheswaran, L. Perrière, A. Ueno, I. Guillot, J.P. Couzinié, G. Dirras, Materialia 4 (2018) 348–360.
[42] O.N. Senkov, J.M. Scott, S.V. Senkova, F. Meisenkothen, D.B. Miracle, C.F. Woodward, J. Mater. Sci. 47 (2012) 4062–4074.
[43] O.N. Senkov, J.M. Scott, S.V. Senkova, D.B. Miracle, C.F. Woodward, J. Alloy. Compd. 509 (2011) 6043–6048.
[44] S. Chen, W. Li, F. Meng, Y. Tong, H. Zhang, K.K. Tseng, J.W. Yeh, Y. Ren, F. Xu, Z. Wu, P.K. Liaw, Scr. Mater. 200 (2021) 113919.
[45] C.C. Juan, M.H. Tsai, C.W. Tsai, W.L. Hsu, C.M. Lin, S.K. Chen, S.J. Lin, J.W. Yeh, Mater. Lett. 184 (2016) 200–203.
[46] G.E. Dieter, D.J. Bacon, Mechanical Metallurgy, McGraw-Hill, New York, 1986.
[47] T.L. Anderson, Fracture Mechanics: Fundamentals and Applications, CRC Press, Boca Raton, FL, 2017.
[48] S. Suresh, R.O. Ritchie, Eng. Fract. Mech. 18 (1983) 785–800.
[49] P.M. Scott, T.W. Thorpe, D.R.V. Silvester, Corros. Sci. 23 (1983) 559–575.
[50] R.O. Ritchie, Int. J. Fract. 100 (1999) 55–83.
[51] R.O. Ritchie, Mater. Sci. Eng. A 103 (1988) 15–28.
[52] P.P. Milella, P.P. Milella, in: Fatigue and Corrosion in Metals, Springer Milan, Milano, 2013, pp. 73–108.
[53] L. Lilensten, J.P. Couzinié, L. Perrière, A. Hocini, C. Keller, G. Dirras, I. Guillot, Acta Mater. 142 (2018) 131–141.
[54] W. Carrington, K.F. Hale, D. McLean, N.P. Allen, Proc. R. Soc. Lond. Ser. A 259 (1960) 203–227.
[55] W.Q. Meeker, L.A. Escobar, Phys. Rev. E 65 (2002) 067102.
[56] J. Schijve, Fatigue Fract. Eng. Mater. Struct. 16 (8) (1993) 851–859.
[57] H. Jia, G. Wang, S. Chen, Y. Gao, W. Li, P.K. Liaw, Prog. Mater. Sci. 98 (2018) 168–248.
[58] O. Basquin, Proc. Am. Soc. Test Mater. (1910) 625–630.
[59] W. Li, S. Chen, P.K. Liaw, Scr. Mater. 187 (2020) 68–75.
[60] K.N. Smith, T. Topper, P. Watson, J. Mater. 5 (1970) 767–778.
[61] H. Ishii, T. Kawarazaki, Y. Fujimura, Metall. Trans. A 15 (1984) 679–691.
[62] M.E. Launey, R.O. Ritchie, Adv. Mater. 21 (2009) 2103–2110.
[63] B. Gludovatz, M.D. Demetriou, M. Floyd, A. Hohenwarter, W.L. Johnson, R.O. Ritchie, Proc. Natl. Acad. Sci. 110 (2013) 18419.
[64] B. Cotterell, J.R. Rice, Int. J. Fract. 16 (1980) 155–169.
[65] S. Suresh, Metall. Trans. A 16 (1985) 249–260.
[66] S. Suresh, R.O. Ritchie, Metall. Trans. A 13 (1982) 1627–1631.
[67] G.T. Gray, J.C. Williams, A.W. Thompson, Metall. Trans. A 14 (2) (1983) 421–433.
[68] R.D. Carter, E.W. Lee, E.A. Starke, C.J. Beevers, Metall. Trans. A 15 (1984) 555.
[69] V.B. Dutta, S. Suresh, R.O. Ritchie, Metall. Mater. Trans. A 15 (1984) 1193–1207.
[70] S. Suresh, G.F. Zamiski, D.R.O. Ritchie, Metall. Mater. Trans. A 12 (1981) 1435–1443.
[71] G.R. Irwin, Onset of Fast Crack Propagation in High Strength Steel and Aluminum Alloys, Naval Research Lab., Washington DC, 1956.
[72] Y. Mutoh, A.A. Korda, Y. Miyashita, T. Sadasue, Mater. Sci. Eng. A 468-470 (2007) 114–119.
[73] S. Suresh, Eng. Fract. Mech. 18 (1983) 577–593.
[74] A.A. Korda, Y. Mutoh, Y. Miyashita, T. Sadasue, S.L. Mannan, Scr. Mater. 54 (2006) 1835–1840.
[75] S. Horibe, R. Hirahara, Acta Metall. Mater. 39 (1991) 1309–1317.
[76] C. Laird, G.C. Smith, Philos. Mag. 7 (1962) 847–857.
[77] B. Chen, S. Li, H. Zong, X. Ding, J. Sun, E. Ma, P. Natl. Acad. Sci. 117 (2020) 16199.
[78] Y. Bu, Y. Wu, Z. Lei, X. Yuan, H. Wu, X. Feng, J. Liu, J. Ding, Y. Lu, H. Wang, Z. Lu, W. Yang, Mater. Today 46 (2021) 28–34.
[79] H. Huang, Y. Wu, J. He, H. Wang, X. Liu, K. An, W. Wu, Z. Lu, Adv. Mater. 29 (30) (2017) 1701678.
[80] R. Schuller, U. Karr, D. Irrasch, M. Fitzka, M. Hahn, M. Bacher-Höchst, H. Mayer, J. Mater. Sci. 50 (2015) 5514–5523.
[81] T. Sakai, Y. Sato, Y. Nagano, M. Takeda, N. Oguma, Int. J. Fatigue 28 (2006) 1547–1554.